

Gell-Mann-Low criticality in neural networks

Lorenzo Tiberi^{1,2,*}, Jonas Stapmanns^{1,2,*}, Tobias Kühn³, Thomas Luu⁴, David Dahmen¹, and Moritz Helias^{1,2}

¹*Institute of Neuroscience and Medicine (INM-6) and Institute for Advanced Simulation (IAS-6) and JARA-Institute Brain Structure-Function Relationships (INM-10), Jülich Research Centre, Jülich, Germany*

²*Institute for Theoretical Solid State Physics, RWTH Aachen University, 52074 Aachen, Germany*

³*Laboratoire de Physique de l'Ecole Normale Supérieure, ENS, Université PSL, CNRS, Sorbonne Université, Université de Paris, F-75005 Paris, France and*

⁴*Institut für Kernphysik (IKP-3), Institute for Advanced Simulation (IAS-4) and Jülich Center for Hadron Physics, Jülich Research Centre, Jülich, Germany*

Criticality is deeply related to optimal computational capacity. The lack of a renormalized theory of critical brain dynamics, however, so far limits insights into this form of biological information processing to mean-field results. These methods neglect a key feature of critical systems: the interaction between degrees of freedom across all length scales, which allows for complex nonlinear computation. We present a renormalized theory of a prototypical neural field theory, the stochastic Wilson-Cowan equation. We compute the flow of couplings, which parameterize interactions on increasing length scales. Despite similarities with the Kardar-Parisi-Zhang model, the theory is of a Gell-Mann-Low type, the archetypal form of a renormalizable quantum field theory. Here, nonlinear couplings vanish, flowing towards the Gaussian fixed point, but logarithmically slowly, thus remaining effective on most scales. We show this critical structure of interactions to implement a desirable trade-off between linearity, optimal for information storage, and nonlinearity, required for computation.

Criticality and information processing are deeply related: Statistical descriptions of the hardest-to-solve combinatorial optimization problems, for example, are right at the edge of a phase transition [1, 2]. Also brain activity shows criticality [3, 4], which may optimize the network's computational properties. Among these, long spatio-temporal correlations support information storage and transmission, while rich collective and nonlinear dynamics allow degrees of freedom to cooperatively perform complex signal transformations [5].

A multitude of critical processes could lie behind critical brain dynamics. Thanks to the universality paradigm of statistical physics, however, their macroscopic behavior is organized into few classes, distinguished by only generic properties, like the system's dimension, the nature of the degrees of freedom, as well as symmetries and conservation laws [6, 7]. Identifying the universality classes implemented by neural networks and finding their distinctive features is key to understanding if and how the brain exploits criticality to perform computation.

Theoretical analysis of critical brain dynamics is, however, so far restricted to mean-field methods. These partly explain why memory, dynamic range and signal separation are optimal at a critical point [8–10]. Still, a fundamental aspect of critical computation is inaccessible to these methods: the nonlinear interaction between degrees of freedom across all length scales. By approximating fluctuations as Gaussian, mean-field theory can study only the linear response of individual modes to stimuli. But a single, uncoupled mode can solve only simple computational tasks. In fact, this approximation only holds if nonlinear interactions, albeit necessary for

computation, are irrelevant on macroscopic scales. Thus, mean-field criticality is a special case, in fact the simplest but also the most restricted kind of criticality the brain could possibly implement. Uncovering different kinds of criticality requires more sophisticated methods.

In this letter we analyze criticality in the stochastic Wilson-Cowan rate model, a prototypical model of brain dynamics [11–13]. We use the non-equilibrium Wilsonian renormalization group to go beyond mean-field analysis [6, 7]. This technique tracks the flow of effective nonlinear couplings as one describes the system on gradually increasing length scales. This exposes the type of criticality featured by the system and its relevance for computation. The model is studied under a continuous stream of external inputs, as typical for interconnected brain areas [14, 15]. While critical activity in networks driven by sparse inputs is well described by branching processes [3, 16] belonging to the universality class of mean-field directed percolation [17], it is still unclear whether constantly driven brain networks are able to support criticality at all [18].

We find the Wilson-Cowan model can indeed be critical in this regime. The derived long-range description is very similar to that of the Kardar-Parisi-Zhang model [19]. But while the latter features a strong coupling fixed point, we find a completely different form of criticality: It is of the Gell-Mann-Low type, the archetypal criticality underlying renormalizability of quantum field theories [20][21, Sec. V]. This type of criticality occurs at the upper critical dimension, at which mean-field theory loses validity. We determine this to be $d = 2$, in agreement with the planar organization of cortical networks. Nonlinear couplings decrease only logarithmically slowly, thus remaining effective on practically all length scales. This property implements a desirable balance between a

* L. Tiberi and J. Stapmanns contributed equally to this work

linear behavior and a nonlinear one; the model optimally remembers signals presented in the past, due to its nearly linear dynamics, and at the same time can perform nonlinear classification.

Focusing on the key ingredients of neural networks, that are nonlinear dynamics of their constituents, noisy drive, and spatially localized nonlinear coupling, we consider a neural field following the well-known Wilson-Cowan equation

$$\tau \frac{dh}{dt} = -l(h) + w * f(h) + \sqrt{\tau} I, \quad (1)$$

where $h(x, t)$ is a neural activity field on the space $x \in \mathbb{R}^d$ that evolves in time t on the characteristic time-scale τ . The function l describes intrinsic local dynamics, and f is a nonlinear gain function. The connectivity kernel $w(x - x')$ weighs the input from the neural state at position x' to that at position x , and $*$ is the spatial convolution. Following a common approach [22], the connectivity w is the sum of two Gaussians with widths σ_{\pm} and amplitudes w_{\pm} , with $\text{sign}(w_{\pm}) = \pm 1$, representing excitatory and inhibitory connections. External input from remote brain areas driving the local activity is, for simplicity, modeled as Gaussian white noise with statistics $\langle I(x, t) \rangle = \mu$ and $\langle I(x, t) I(x', t') \rangle = D \delta(x - x') \delta(t - t')$. A microscopic length a characterizes the spatial resolution of the model, thus Eq. (1) is defined on a square lattice with N^d sites and spacing a , eventually taking the limit $N \rightarrow \infty$. Equivalently, momenta are restricted to $|k| < \Lambda := \pi/a$.

The computational properties of the model are later tested in a reservoir computing setting [23]: A linear readout is trained to extract a desired input-output mapping from the neural activity (Fig. 1(a)). Nonlinear interactions are fundamental to achieve complex mappings. We thus want to go beyond mean-field methods and instead track the relevance of nonlinear interactions on gradually increasing length scales.

We make explicit all nonlinear terms in Eq. (1) by Taylor expanding $f(x) = \sum_n f_n x^n$ and likewise l . Also, the momentum dependence of the Fourier transformed coupling kernel $\hat{w}(k) = \sum_{\pm} w_{\pm} (1 - \frac{1}{2} \sigma_{\pm}^2 k^2 + \mathcal{O}(k^4))$ is kept up to second order, enough to expose those terms that characterize the system on a mesoscopic length-scale. We thus obtain, in the spatial domain,

$$\tau \frac{dh}{dt} = \sum_{n=1}^{\infty} (-m_n + g_n \Delta + \mathcal{O}(\Delta^2)) h^n + I, \quad (2)$$

where Δ is the Laplace operator and $\mathcal{O}(\Delta^2)$ denotes all terms proportional to spatial differential operators of order ≥ 4 . Couplings are conveniently renamed $m_n := l_n - f_n \sum_{\pm} w_{\pm}$, characterizing the local dynamics, and $g_n := \frac{1}{2} f_n \sum_{\pm} \sigma_{\pm}^2 w_{\pm}$, quantifying the interaction across space points. Notice μ , l_0 and f_0 , corresponding to a constant input causing $\langle h \rangle \neq 0$, are without loss of generality set to zero (see Supplemental Material).

Temporarily neglecting nonlinearities ($g_n, m_n = 0 \forall n > 1$), the mass term m_1 plays the role of a lower momentum cut-off [21]. This defines the system's spatial ($\propto m_1^{-\frac{1}{2}}$) and temporal ($\propto m_1^{-1}$) correlation lengths, both diverging as $m_1 \rightarrow 0$. Thus $m_1 = 0$ identifies a critical point of the linear model. To include the effect of nonlinearities close to this point, standard expansion methods fail: perturbative corrections diverge due to statistical fluctuations interacting on an infinite range of length scales [21].

To tackle this issue, the renormalization group (RG) [6, 7, 21] performs the integration of fluctuations gradually over momentum scales $\Lambda/\ell < |k| < \Lambda$; progressively increasing the flow parameter $\ell \in [1, \infty)$, we obtain a series of effective field theories, each describing only degrees of freedom on larger length scales, with $k < \Lambda/\ell$. Such theories are defined on the rescaled quantities $k_{\ell} := \ell k$, $t_{\ell} := \ell^{-z} t$, $\hat{h}_{\ell}(k_{\ell}, t_{\ell}) := \ell^{-\zeta} \hat{h}(k, t)$ and $\hat{I}_{\ell}(k_{\ell}, t_{\ell}) := \ell^{\chi} \hat{I}(k, t)$. Rescaling makes all effective field theories look formally equivalent to Eq. (2), differing only by the values of the couplings $m_n(\ell)$ and $g_n(\ell)$, which become ℓ -dependent. This dependence accounts for two effects: The interaction with the integrated out degrees of freedom and the rescaling. The couplings' flow with ℓ therefore characterizes nonlinear interactions on different length scales and, thus, the type of critical behavior featured by the system. For example, the flow running into a fixed point is a characteristic of critical systems and determines their typical scale invariance.

We begin with analyzing the coupling's flow due to rescaling alone. This corresponds to standard dimensional analysis and the mean-field approach, neglecting the contribution of fluctuations. As typical brain networks have a planar organization, we are ultimately interested in the case $d = 2$. We choose $z = 2$, $\zeta = \frac{d+2}{2}$, and $\chi = \frac{d-2}{2}$ so that g_1 , τ , and the input variance D are at a fixed point (i.e. do not rescale). With this choice, for $d \geq 2$ all couplings not appearing explicitly in Eq. (2) rapidly flow to 0 with some negative power of ℓ . These couplings are termed *irrelevant* and can be neglected as the effective theory's reference scale ℓ is increased. The couplings $m_n(\ell) = \ell^{2-(n-1)\frac{d-2}{2}} m_n(1)$ diverge at $d = 2$ as $\sim \ell^2$. They are termed *relevant*, meaning they must be fine-tuned to 0 to be at a fixed point. This fine-tuning here implies balance of inhibitory and excitatory inputs (see Supplemental Material), often observed in brain networks as a necessary condition for criticality [24]. The couplings $g_n(\ell) = \ell^{-(n-1)\frac{d-2}{2}} g_n(1)$ vanish for $d > 2$, $\forall n \geq 2$. For these spatial dimensions, mean-field theory is usually accurate: all nonlinear terms in Eq. (2) are negligible at large scales, thus fluctuations have almost no interactions and can be neglected. Conversely, dimensional analysis predicts $d = 2$ as the upper critical dimension at which the g_n do not scale and are thus termed *marginal*: their flow is driven by fluctuations alone and thus must be investigated with more sophisticated methods, like the RG.

The mean-field analysis above allows us to determine the form of the effective theory describing the critical system at a mesoscopic scale, where irrelevant couplings are negligible

$$\tau \frac{dh}{dt} = \Delta (g_1 h + g_2 h^2 + g_3 h^3) + I. \quad (3)$$

Notice that, at such scales, the field h describes neural populations exchanging activity with nearest neighbors via a diffusive process, as expressed by the Laplace operator Δ [25]. Among the marginal couplings g_n , we keep only the first $n \leq n_0 = 3$. We can assume neural activity to mainly explore a limited range of the gain function [26, 27], which can therefore be locally approximated with a polynomial. We choose $n_0 = 3$ to keep a minimal approach ($n_0 = 2$ cannot be chosen, as Eq. (3) would be unstable). Equation (3) was proposed as an alternative to the Kardar-Parisi-Zhang (KPZ) model [28, 29], both describing the dynamic growth of interfaces. The original KPZ model [19] defines the KPZ universality class, where the interaction flows into a strong-coupling fixed point. Despite the similarities, we show Eq. (3) to exhibit a radically different type of critical behavior.

We start from Eq. (3) to compute the fluctuation-driven part of the couplings' flow. This is conveniently done by mapping Eq. (3) to a field theory by means of the Martin-Siggia-Rose-de Dominicis-Janssen formalism [30–33]. Flow equations are then computed to one-loop order with Feynman diagram techniques, within the framework of the infinitesimal momentum shell Wilsonian RG for non-equilibrium systems [6] (details in Supplemental Material). Notice only g_2 and g_3 are meaningful parameters, as one can rewrite Eq. (3) in dimensionless form by setting τ, g_1, D and a to unity and renaming $\bar{g}_n := (D/g_1)^{\frac{n-1}{2}} \frac{g_n}{g_1}$. We use this convention for the remainder of this letter. Defining $s := (2\pi)^{-1} \ln(\ell)$, the differential flow equations take the form

$$\frac{1}{g_1} \frac{dg_1}{ds} = \frac{3}{2} \bar{g}_3 - \bar{g}_2^2, \quad (4)$$

$$\frac{d\bar{g}_2^2}{ds} = -\frac{27}{2} \bar{g}_3 \bar{g}_2^2 + 7 \bar{g}_2^4, \quad (5)$$

$$\frac{d\bar{g}_3}{ds} = -\frac{15}{2} \bar{g}_3^2 + 14 \bar{g}_3 \bar{g}_2^2 - 4 \bar{g}_2^4, \quad (6)$$

showing that \bar{g}_2 and \bar{g}_3 alone drive the flow. The Laplace operator in front of the nonlinear terms in Eq. (3) protects D, τ and m_n from fluctuation corrections (see Supplemental Material), so their flow is completely determined by the mean-field analysis above. Fig. 1(b) shows the flow vector field in the $\bar{g}_3 - \bar{g}_2^2$ plane. A line $\frac{\bar{g}_2^2}{\bar{g}_3} = \frac{7+\sqrt{145}}{8}$ determines a transition between a diverging and converging behavior.

Below the transition line, the couplings vanish, flowing into the Gaussian fixed point ($\bar{g}_2 = \bar{g}_3 = 0$). Differently than in a mean-field scenario, however, the flow is logarithmically slow in ℓ , a characteristic of marginal

couplings at the upper critical dimension. This means interactions are effectively present on a wide range of length scales. Finite-size systems typically do not even reach the extent beyond which interactions become truly negligible. This is known as Gell-Mann-Low criticality, the archetypal behavior underlying renormalizability of quantum field theories, such as Quantum Electrodynamics (QED) [20][21, Sec. V]. Here one observes nonlinearities that shape non-trivial electro-magnetic interactions on a wide range of scales. A difference to a prototypical Gell-Mann-Low theory, however, is that the flow is driven by the pair of marginal couplings (\bar{g}_2, \bar{g}_3) , rather than by a single coupling, which for QED is the charge. At large scales, the power law scaling exponents z, ζ , and χ maintain their mean-field values, since interactions eventually vanish. However, logarithmic corrections must be included due to the slowness of the flow. One example of this effect can be seen in the scaling of the variance $\langle h^2 \rangle$ as a function of N shown in Fig. 1(d). These logarithmic corrections may also be mistaken as different power law exponents, which depend on the system's dynamical state, rather than being universal. Thus they can lead to small, state-dependent shifts in measured scaling exponents with respect to their mean-field value (see Supplemental Material).

As previously noted by [29], the infinite number of marginal couplings g_n in principle allows for the existence of an infinite number of fixed points. Determining analytically whether these are attractive, though, has never been done due to the technical difficulty of the task. In neglecting $g_n, \forall n > 3$, we are implicitly assuming the Gaussian fixed point is stable, with a sufficiently large basin of attraction to attract the flow from any initial g_n . We therefore test the validity of the flow equations numerically, by integrating Eq. (3) with the Euler-Maruyama algorithm [34] (additional details in Supplemental Material). Measurements are restricted to $\bar{g}_2^2 < 3\bar{g}_3$ (Fig. 1(b)), due to the occurrence of an unphysical bi-stable regime above such boundary (Supplemental Material).

We simulate systems of increasing size N , which limits the extent of correlations. By measuring correlation functions of the neural field h , we extract the value of the flown couplings at different length scales $\ell = \frac{N}{2}$ and initial conditions, shown in Fig. 1(b). Below the transition line, we observe good qualitative agreement between the measured and predicted flow. Quantitative departures from predictions are expected, given the approximation made to one-loop order in fluctuations and to third order in the expansion of f . This approximation is good enough, given our goal to qualitatively confirm the running of the flow towards the Gaussian fixed point. Higher orders could be easily included, if needed, at the relatively low cost of computing more Feynman diagrams.

Above the transition line instead, our approximation leads to a divergence of the flow. This could signal the presence of a strong coupling fixed point, into which the flow eventually runs. This occurs, for example, in

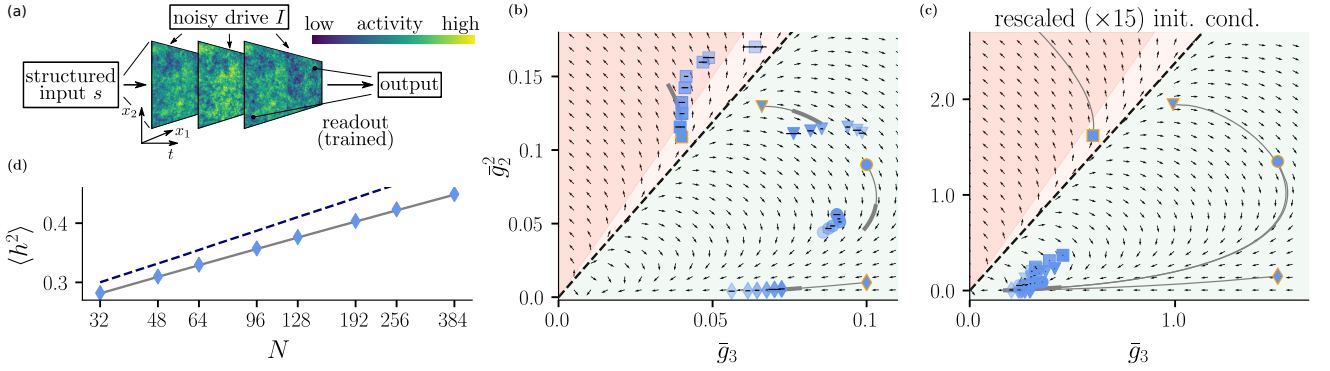


Figure 1. Phase diagram and flow of couplings. (a) Scheme of the model. (b) and (c): Direction of flow (arrows) in the $\bar{g}_3 - \bar{g}_2^2$ plane, as defined by Eq. (5) and Eq. (6). The transition line (black, dashed) separates the plane in a converging (green) and diverging region (red). Region of non-physical bi-stable regime in darker red (see Supplemental Material). Blue markers represent the measured flow of couplings at $\ell = \frac{N}{2}$, with $N \in \{32, 48, 64, 96, 128, 192\}$ (dark to light shading; squares in (b) also include $N = 256, 384$ for different initial conditions (yellow edge). Gray solid lines (thicker within the range of simulated ℓ) represent the corresponding predicted flow. (d): Measured variance (blue diamonds) as a function of N for $\bar{g}_3 = 0.1$ and $\bar{g}_2^2 = 0.01$ ($\bar{g}_2^2 \ll \bar{g}_3$ regime), compared against the linear case (dashed, dark blue line) and prediction (gray, solid line).

the KPZ model for $d \geq 3$, where an analogous transition point exists [35]. Differently, however, our measurements in Fig. 1(b) suggest the flow still heads towards the Gaussian fixed point, making a u-turn similar to when starting close and below the transition line. This is confirmed in Fig. 1(c), showing the flow for larger initial values of the couplings. The flow is then subject to a stronger drive in its initial transient, thus spanning a longer trajectory within the same range of ℓ . These measurements thus suggest that, regardless of the initial condition, after an initial transient the flow always runs into the $\bar{g}_3 \gg \bar{g}_2^2$ region, heading towards the Gaussian fixed point. Luckily, this region is where the flow equations in the given approximation yield reliable quantitative predictions. This is exemplified by the measured neural field variance $\langle h^2 \rangle$ as a function of N being well predicted by theory (Fig. 1(d)). In the limit $N \rightarrow \infty$, we predict $\langle h^2 \rangle \sim (4\pi g_1(\ell))^{-1} \ln(\frac{N}{2})$, with $\ell \stackrel{!}{=} \frac{N}{2}$ (see Supplemental Material). The ℓ -dependence of g_1 shows a logarithmic correction with respect to the linear case, in which $g_1(\ell) = 1 \forall \ell$.

We have so far demonstrated that the system showcases criticality of the Gell-Mann-Low kind. The question remains on why, among types of criticality, this one would be especially beneficial for computation. Criticality optimizes desirable computational properties; still, these may strive for a balance between a linear behavior, optimal for storage and transmission of information, and a nonlinear one, necessary for computation. The Gell-Mann-Low criticality implements such a balance by sitting in-between a mean-field and strong coupling fixed point scenario. We exemplify this by training the system Eq. (3) to solve example tasks by what is known as reservoir computing (Fig. 1(a)) [23]: A structured input s is fed at some time t_{in} in the form of a perturbation $h(x, t_{in}) + s(x)$. At a later time t_{out} , a linear readout $\sum_x W(x) h(x, t_{out})$ is taken and the parameters $W(x)$

are trained with gradient descent (task-specific details in Supplemental Material).

We first focus on memory; for concreteness, consider the Fischer memory curve [36]. In the linear case, it is expected to be optimal, and to decay with time as t^{-2} . Being a global feature, involving the system as a whole on long time scales, it benefits from the system's closeness to linear dynamics. Indeed, since nonlinearities vanish on a global length scale, as opposed to a strong coupling fixed point scenario, they do not worsen the power law decay found in the optimal linear case; rather they cause only small logarithmic corrections. Inspired by these theoretical grounds, we train N^2 linear readouts to reconstruct a Gaussian-shaped input at some time t after injection, recording the reconstruction accuracy (Fig. 2(a)). As expected, increasing the strength of nonlinearities, the accuracy's power law exponent does not deviate appreciably from the linear case: performance is only worsened by a constant shift in double logarithmic scale.

In contrast to a strict mean-field scenario, nonlinearities are, however, still relevant on most length scales other than the very macroscopic ones, thus allowing the system's degrees of freedom to interact and to collectively perform computation. We exemplify this by training two linear readouts to correctly classify the parity of 3-bit strings. The task is not linearly separable: no plane can correctly separate the strings in the two categories (Fig. 2(c)). Nonlinear dynamics are necessary to expand the input's dimensionality, thus making linear separation possible. The input string's n -th bit is encoded by the sign of a perturbation of the Fourier mode of momentum $k_n = (\pi - n 4\pi/N) \hat{e}_1$, right below the high momentum cut-off π . The linear readout is taken on a low-pass filtered h , restricted to momenta $< |k_3|$. Thus nonlinear dynamics are further necessary to transfer information from the input to the readout modes. Fig. 2(b) indeed shows successful training. Performance decays on a time

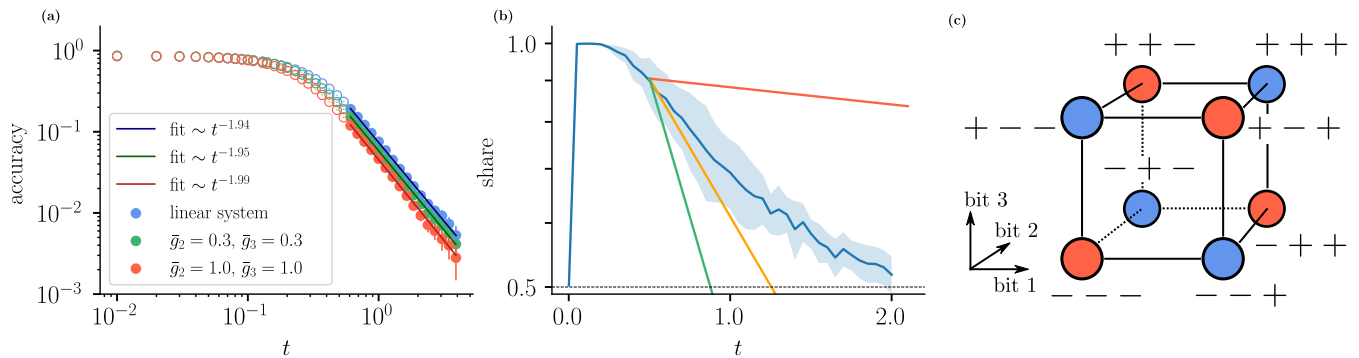


Figure 2. Examples of computation. (a) Memory: reconstruction accuracy over time of a Gaussian input for different strengths of the nonlinearities (legend). Values range from 0 (complete forgetting) to 1 (perfect reconstruction). (b) Classification: Share of correctly classified 3-bit strings (blue line) and standard deviation across repeated trainings (blue area). Other curves decay with the time-scale of the slowest (red), middle (orange) and fastest (green) modes available at readout. (c) Spatial position of the 3-bit strings, colored by their parity.

scale between the characteristic scales of the slowest and fastest modes, suggesting their collective interaction to be employed to perform the task. The modes' response shown in the Supplemental Material further imply this, see Fig. S3.

In conclusion, we furnish the tools, a renormalized theory of neural network dynamics, to uncover the structure of nonlinear interactions across scales, so far inaccessible by mean-field methods. This framework opens the door to explore many other forms of criticality, beyond mean-field, that neural networks might implement, and to quantitatively address nonlinear signal transformations at a dynamical critical point. Applying the methods to the stochastic Wilson-Cowan model, we find a new form of criticality, which is robust to the biologically plausible external drive. At the relevant dimension $d = 2$, critical behavior ceases to be mean-field, being instead of the Gell-Mann-Low kind. Most notably, nonlinear couplings, fundamental for computation, have a logarithmically slow, rather than power-law vanishing flow. We argue that this supports a computationally optimal balance between linear and nonlinear dynamics. The RG methodology and the concept of Gell-Mann-Low criticality are generally applicable to any stochastic dynamical

system. We thus foresee applications to computation-oriented, possibly more complex models, both biological and artificial. For example, Gell-Mann-Low criticality could naturally account for the variability in critical exponents observed in the context of neural avalanches [37, 38]. The link between neural field theory, the KPZ model central to non-equilibrium statistical physics, and quantum field theory presents a stepping stone to transfer expertise from these fields, where RG methods are widely used.

ACKNOWLEDGMENTS

We are grateful for various helpful discussions with Carsten Honerkamp. This project has received funding from the European Union's Horizon 2020 Framework Programme for Research and Innovation under Specific Grant Agreement No. 945539 (Human Brain Project SGA3); the Helmholtz Association: Young Investigator's grant VH-NG-1028; the Jülich-Aachen Research Alliance Center for Simulation and Data Science (JARA-CSD) School for Simulation and Data Science (SSD); L.T. received funding as Vernetzungsdoktorand: "Collective behavior in stochastic neuronal dynamics".

-
- [1] P. Cheeseman, B. Kanefsky, and W. M. Taylor, in *Proceedings of the 12th International Joint Conference on Artificial Intelligence - Volume 1* (Morgan Kaufmann Publishers Inc., San Francisco, CA, USA, 1991), IJ-CAI'91, pp. 331–337, ISBN 1558601600.
 - [2] L. Saitta, A. Giordana, and A. Cornuéjols, *Phase Transitions in Machine Learning* (Cambridge University Press, 2011).
 - [3] J. M. Beggs and D. Plenz, *J. Neurosci.* **23**, 11167 (2003).
 - [4] D. R. Chialvo, *Nature Physics* **6**, 744 (2010), ISSN 1745-2481, number: 10 Publisher: Nature Publishing Group.
 - [5] C. G. Langton, *Physica D: Nonlinear Phenomena* **42**, 12 (1990).
 - [6] P. C. Hohenberg and B. I. Halperin, *Rev. Mod. Phys.* **49**, 435 (1977).
 - [7] U. C. Täuber, *Critical dynamics: a field theory approach to equilibrium and non-equilibrium scaling behavior* (Cambridge University Press, 2014), ISBN 9780521842235.
 - [8] N. Bertschinger and T. Natschläger, *Neural Computation* **16**, 1413 (2004).
 - [9] N. Bertschinger, T. Natschläger, and R. A. Legenstein, in *Advances in neural information processing systems* (2005), pp. 145–152.

- [10] O. Kinouchi and M. Copelli, *Nature Physics* **2**, 348 (2006), ISSN 1745-2481, number: 5 Publisher: Nature Publishing Group.
- [11] H. R. Wilson and J. D. Cowan, *Biophys. J.* **12**, 1 (1972).
- [12] H. R. Wilson and J. D. Cowan, *Kybernetik* **13**, 55 (1973), ISSN 1432-0770.
- [13] A. Destexhe and T. J. Sejnowski, *Biol. Cybern.* **101**, 1 (2009).
- [14] A. Schüz and V. Braitenberg, in *Cortical Areas: Unity and Diversity*, edited by A. Schüz and R. Miller (Taylor and Francis, 2002), chap. 16, pp. 377–385.
- [15] A. Destexhe, M. Rudolph, and D. Pare, *Nat. Rev. Neurosci.* **4**, 739 (2003).
- [16] C. Haldeman and J. M. Beggs, *Phys. Rev. Lett.* **94**, 058101 (2005).
- [17] M. Henkel, H. Hinrichsen, and S. Lübeck, *Non-Equilibrium Phase Transitions: Volume 1: Absorbing Phase Transitions* (Springer Netherlands, 2008), ISBN 978-1-4020-8764-6, URL <https://www.springer.com/gp/book/9781402087646>.
- [18] L. J. Fosque, R. V. Williams-García, J. M. Beggs, and G. Ortiz, *Phys. Rev. Lett.* **126**, 098101 (2021).
- [19] M. Kardar, G. Parisi, and Y.-C. Zhang, *Phys. Rev. Lett.* **56**, 889 (1986).
- [20] M. Gell-Mann and F. E. Low, *Phys. Rev.* **95**, 1300 (1954).
- [21] K. G. Wilson, *Rev. Mod. Phys.* **47**, 773 (1975).
- [22] B. Ermentrout, *Reports on Progress in Physics* **61**, 353 (1998).
- [23] M. Lukoševičius and H. Jaeger, *Computer Science Review* **3**, 127 (2009).
- [24] W. L. Shew, H. Yang, T. Petermann, R. Roy, and D. Plenz, *J. Neurosci.* **29**, 15595 (2009).
- [25] S. di Santo, P. Villegas, R. Burioni, and M. A. Munoz, *Proceedings of the National Academy of Sciences* **115**, E1356 (2018), ISSN 0027-8424.
- [26] S. Ostojic and N. Brunel, *PLOS Comput. Biol.* **7**, e1001056 (2011).
- [27] A. Roxin, N. Brunel, D. Hansel, G. Mongillo, and C. van Vreeswijk, *J. Neurosci.* **31**, 16217 (2011).
- [28] S. Pavlik, *Zh. Eksp. Teor. Fiz.* **106**, 553 (1994).
- [29] N. V. Antonov and A. N. Vasiliev, *Zh. Èksp. Teor. Fiz.* **81**, 485 (1995).
- [30] P. Martin, E. Siggia, and H. Rose, *Phys. Rev. A* **8**, 423 (1973).
- [31] C. De Dominicis, *J. Phys. Colloques* **37**, C1 (1976).
- [32] J. A. Hertz, Y. Roudi, and P. Sollich, *Journal of Physics A: Mathematical and Theoretical* **50**, 033001 (2017).
- [33] M. Helias and D. Dahmen, *Statistical Field Theory for Neural Networks*, vol. 970 (Springer International Publishing, 2020).
- [34] P. E. Kloeden and E. Platen, *Numerical Solution of Stochastic Differential Equations* (Springer, Berlin, 1992).
- [35] H. C. Fogedby and W. Ren, *Phys. Rev. E* **80**, 041116 (2009).
- [36] S. Ganguli, D. Huh, and H. Sompolinsky, *Proc. Nat. Acad. Sci. USA* **105**, 18970 (2008).
- [37] A. J. Fontenele, N. A. P. de Vasconcelos, T. Feliciano, L. A. A. Aguiar, C. Soares-Cunha, B. Coimbra, L. Dalla Porta, S. Ribeiro, A. J. a. Rodrigues, N. Sousa, et al., *Phys. Rev. Lett.* **122**, 208101 (2019).
- [38] T. T. A. Carvalho, A. J. Fontenele, M. Girardi-Schappo, T. Feliciano, L. A. A. Aguiar, T. P. L. Silva, N. A. P. de Vasconcelos, P. V. Carelli, and M. Copelli, *Frontiers in Neural Circuits* **14**, 83 (2021), ISSN 1662-5110.

Supplemental material: Gell-Mann-Low criticality in neural networks

Lorenzo Tiberi^{1,2,*}, Jonas Stapmanns^{1,2,*}, Tobias Kühn³, Thomas Luu⁴, David Dahmen¹, and Moritz Helias^{1,2}

¹*Institute of Neuroscience and Medicine (INM-6) and Institute for Advanced Simulation (IAS-6) and JARA-Institute Brain Structure-Function Relationships (INM-10), Jülich Research Centre, Jülich, Germany*

²*Institute for Theoretical Solid State Physics, RWTH Aachen University, 52074 Aachen, Germany*

³*Laboratoire de Physique de l'Ecole Normale Supérieure, ENS, Université PSL, CNRS, Sorbonne Université, Université de Paris, F-75005 Paris, France and*

⁴*Institut für Kernphysik (IKP-3), Institute for Advanced Simulation (IAS-4) and Jülich Center for Hadron Physics, Jülich Research Centre, Jülich, Germany*

I. MAPPING INTO A FIELD THEORY

Stochastic differential equations, the likes of Eq. (1), can be equivalently represented in terms of a field theory by means of the Martin-Siggia-Rose-de Dominicis-Janssen (MSRDJ) formalism [1–4]. Here we give the field theory's action that can be derived with this mapping, as well as its associated Feynman rules [5]. The latter are used to compute the flow equations, as well as the analytical predictions that are compared against numerical simulations.

Field theory The statistics of the neural field h are described in terms of a moment generating functional

$$Z[j, \tilde{j}] = \int \mathcal{D}h \mathcal{D}\tilde{h} \exp \left(S(h, \tilde{h}) + j^T h + \tilde{j}^T \tilde{h} \right), \quad (\text{S1})$$

defined by a path integral over the field h and an auxiliary field \tilde{h} , with the action

$$S(h, \tilde{h}) = \tilde{h}^T \left(\frac{d}{dt} h + l(h) - w * f(h) \right) + W_I(-\tilde{h}), \quad (\text{S2})$$

where we used the notation $f^T g := \int d^d x dt f(x, t) g(x, t)$ and we have set $\tau = 1$ in Eq. (1), corresponding to a trivial rescaling of time. Here, W_I is the cumulant generating functional of the random input I . In our case

$$W_I(-\tilde{h}) = -\mu^T \tilde{h} + \frac{D}{2} \tilde{h}^T \tilde{h} \quad (\text{S3})$$

with $\mu(r, t) := \mu = \text{const.}$ Moments of h and \tilde{h} correspond to functional derivatives of Z with respect to n source fields j and m fields \tilde{j} . Specifically

$$\begin{aligned} \frac{\partial Z}{\partial j(x_1, t_1) \dots \partial j(x_n, t_n) \partial \tilde{j}(x'_1, t'_1) \dots \partial \tilde{j}(x'_m, t'_m)} \Big|_{j, \tilde{j}=0} &= \frac{\partial \langle h(x_1, t_1) \dots h(x_n, t_n) \rangle}{\partial \tilde{j}(x'_1, t'_1) \dots \partial \tilde{j}(x'_m, t'_m)} \Big|_{\tilde{j}=0} \\ &= \langle h(x_1, t_1) \dots h(x_n, t_n) \tilde{h}(x'_1, t'_1) \dots \tilde{h}(x'_m, t'_m) \rangle. \end{aligned} \quad (\text{S4})$$

Setting the number of \tilde{j} -derivatives to $m = 0$, one can thus compute moments of the neural field h . Additionally, differentiating m times with respect to \tilde{j} allows one to compute the m -th order response function of such moments to a small perturbation in the system's input. This can be seen from the fact that, in Eq. (S1), both μ and \tilde{j} couple linearly with \tilde{h} . Thus $-\tilde{j}$ represents an additive perturbation to the average input μ . Notice that Eq. (S4) relates derivatives in \tilde{j} to moments of \tilde{h} , thus the statistics of the auxiliary field \tilde{h} has the physical interpretation of describing the system's response to stimuli. For this reason \tilde{h} is usually called response field. By construction instead, all moments of the field h alone ($n = 0$ derivatives by j) vanish [6, p. 38].

* L. Tiberi and J. Stapmanns contributed equally to this work

Feynman rules The Feynman rules for the field theory Eq. (S2) are given in terms of propagators and interaction vertices in momentum and frequency domain. We denote by H and \tilde{H} the Fourier transformed fields h and \tilde{h} in both frequency and momentum space. Propagators are given by inverting the second order functional derivative of the action

$$\begin{pmatrix} \Delta_{HH}(k, \omega) & \Delta_{H\tilde{H}}(k, \omega) \\ \Delta_{\tilde{H}\tilde{H}}(-k, -\omega) & \Delta_{\tilde{H}H}(k, \omega) \end{pmatrix} \begin{pmatrix} \frac{\partial^2 S}{\partial H(k, \omega) \partial H(k', \omega')} & \frac{\partial^2 S}{\partial H(k, \omega) \partial \tilde{H}(k', \omega')} \\ \frac{\partial^2 S}{\partial \tilde{H}(k, \omega) \partial H(k', \omega')} & \frac{\partial^2 S}{\partial \tilde{H}(k, \omega) \partial \tilde{H}(k', \omega')} \end{pmatrix}_{H, \tilde{H}=0} = -(2\pi)^{d+1} \delta(k + k') \delta(\omega + \omega'),$$

which gives explicitly

$$\Delta_{H\tilde{H}}(k, \omega) = \frac{-1}{i\omega + m_1 + g_1 k^2 + \mathcal{O}(k^4)} \quad := \quad \text{Diagram: } H \xleftarrow{k, \omega} \tilde{H} \quad (\text{S5})$$

$$\Delta_{HH}(k, \omega) = \frac{D}{\omega^2 + (m_1 + g_1 k^2 + \mathcal{O}(k^4))^2} \quad := \quad \text{Diagram: } H \xleftrightarrow{k, \omega} H \quad (\text{S6})$$

and $\Delta_{\tilde{H}\tilde{H}} = 0$. Here i denotes the imaginary unit. The Feynman diagram representation of both propagators is given on the *r.h.s.* of equations Eq. (S5) and Eq. (S6). Denoting with \hat{h} and $\hat{\tilde{h}}$ the Fourier transformed fields in momentum space alone, the propagators can also be written as a function of time and momentum as

$$\Delta_{\hat{\tilde{h}}\hat{h}}(k, t) = -\theta(t) \exp(-(m_1 + g_1 k^2)t), \quad (\text{S7})$$

$$\Delta_{\hat{h}\hat{h}}(k, t) = \frac{D}{2(m_1 + g_1 k^2)} \exp(-(m_1 + g_1 k^2)|t|). \quad (\text{S8})$$

The interaction vertices are defined by higher order functional derivatives of S

$$\frac{1}{n!} \frac{\partial S}{\partial \tilde{H}(k_1, \omega_1) \partial H(k_2, \omega_2) \dots \partial H(k_{n+1}, \omega_{n+1})} \Big|_{H, \tilde{H}=0} = (m_n + g_n k_1^2 + \mathcal{O}(k_1^2)) (2\pi)^{d+1} \delta\left(\sum_{i=1}^{n+1} k_i\right) \delta\left(\sum_{i=1}^{n+1} \omega_i\right)$$

$$:= \quad \text{Diagram: } k_1, \omega_1 \text{ --- } \text{wavy line} \text{ --- } k_2, \omega_2, \dots, k_{n+1}, \omega_{n+1} \quad (\text{S9})$$

where wiggly lines represent amputated legs. The couplings $m_n := l_n - f_n \sum_{\pm} w_{\pm}$ and $g_n := \frac{1}{2} f_n \sum_{\pm} \sigma_{\pm}^2 w_{\pm}$ are defined as in the main text by the expansion of f and l around $h = 0$, that is $f_n := \frac{1}{n!} \frac{d^n f}{dh^n} |_{h=0}$ and $l_n := \frac{1}{n!} \frac{d^n l}{dh^n} |_{h=0}$.

Non-zero mean of the field In the main text, we claim μ , l_0 and f_0 can in all generality be set to zero, corresponding to $\langle h \rangle = 0$. We here justify this statement. Notice the Feynman rules above are derived expanding the action around $h = 0$. In general, non-vanishing μ , l_0 and f_0 correspond to a constant input, causing $\langle h \rangle = \text{const} \neq 0$. It is in general possible to expand the action around a non-vanishing constant mean $h = \langle h \rangle$. This gives Feynman rules formally equivalent to Eqs. (S5)-(S9), with the only difference that the couplings m_n and g_n are defined in terms of the expansion of f and l around $h = \langle h \rangle$, that is $f_n := \frac{1}{n!} \frac{d^n f}{dh^n} |_{h=\langle h \rangle}$ and $l_n := \frac{1}{n!} \frac{d^n l}{dh^n} |_{h=\langle h \rangle}$. The loopwise expansion of the effective action [5], for example, obeys these rules and indeed allows the study of fluctuations of the shifted field $\delta h := h - \langle h \rangle$. In general, the exact value of the couplings m_n and g_n therefore depends on the mean $\langle h \rangle$, which in turn depends on the input mean μ . We notice, however, that this is of no concern for a renormalization group analysis. The latter is indeed not interested in knowing *a priori* the exact value of the couplings in the microscopic theory. Instead, experiments are used to *a posteriori* determine the value of the effective couplings defining the effective theory at a certain length scale. One is rather interested in knowing the couplings' flow for any initial condition, that is for any possible value of the couplings in the microscopic theory. In this way one can indeed find out which of those couplings are relevant in defining the effective theory and need to be measured. Notice that the nature of the flow is determined by the interaction's structure of the system, which is the same given by Eqs. (S5)-(S9) regardless of the point of expansion $h = \langle h \rangle$. For this reason, in the main text we set in all generality μ , l_0 and f_0 to zero, corresponding to $\langle h \rangle = 0$.

State-dependent power laws In a Gell-Mann Low type of flow [7][8, Sec. V], the Gaussian fixed point is reached so slowly that on many, even large length scales the effective couplings are non-zero. Also, their slow flow can make them appear to be approximately constant over a range of length scales. This implies that the universality of a fixed point

is in practice never reached. In particular, the universal mean-field scaling exponents can receive small corrections, which depend on the value taken by the flown couplings at the scale experiments are made. Indeed, consider an experiment made on a range of scales over which $\bar{g}_n(\ell) \sim \bar{g}_n^*$ for $n = 2, 3$ appear as approximately constant, because of their slow flow. Then the flow equation Eq. (4) tells us that $g_1(\ell) \propto \ell^{2\epsilon}$ with $2\epsilon = \frac{3}{2}\bar{g}_3^* - \bar{g}_2^{*2}$. To actually keep $g_1 \stackrel{!}{=} 1$ at a fixed point, the mean-field scaling exponents therefore need to modify as $\chi \rightarrow \chi + \epsilon, \zeta \rightarrow \zeta - \epsilon, z \rightarrow z - 2\epsilon$. Notice this modification is parameterized by ϵ , which depends on the value taken by the flown couplings. This is not universal and depends on both the scale at which experiments are made and the initial condition for the flow, that is the value of the couplings in the microscopic theory. It is interesting to notice how, in our model, this initial value of the couplings depends on the state of the system, in particular on the parameters characterizing the noisy drive coming from other brain areas. Specifically, the variance D enters directly in the definition of the dimensionless couplings $\bar{g}_n := (D/g_1)^{\frac{n-1}{2}} \frac{g_n}{g_1}$. The input mean μ also determines the value of g_n by controlling the value of the mean $\langle h \rangle$ around which the field theory is Taylor expanded to define the couplings (see paragraph above).

Balance of inhibitory and excitatory connections at criticality As stated in the main text, the model is at a critical point for $m_n := l_n - f_n \sum_{\pm} w_{\pm} = 0$. We show that this implies a balance of inhibitory and excitatory inputs to a neuron. We can assume $l(\bar{h}) \ll w_{\pm} f(h)$, which means that the rate at which neural activity decays is much smaller than that at which it is updated by new inputs, whether excitatory or inhibitory. Then, at first order, the condition for criticality can be satisfied by the vanishing of the second term alone in the definition of m_n , that is for $|w_+| = |w_-|$. Recall w_{\pm} are the amplitudes, of opposite sign, of the normalized Gaussians modeling the strength of inhibitory and excitatory connections as a function of distance. Thus their equivalence in absolute value implies that the overall (i.e. integrated over space) strength of inhibitory and excitatory connections is balanced.

II. NUMERICAL SIMULATIONS

Here we give details about the numerical simulation of Eq. (3). First, we present the common ground on which we build the numerical experiments measuring the variance and couplings' flow, as well as the computational tasks. These then have each their own explanatory section. Finally, in the last section we provide the values of the parameters used to produce the figures in the main text.

Numerical simulations are performed integrating a discrete version of Eq. (3) with the Euler-Maruyama algorithm [9]. The equation is simulated in its dimensionless form, thus with $\tau = g_1 = D = a = 1$. The field variable $h(x, t)$ is defined on a square lattice of $N \times N$ sites at space points $x = x_1 \hat{e}_1 + x_2 \hat{e}_2$, with $x_1, x_2 \in \{1, \dots, N\}$ and periodic boundary conditions, and at discrete time points $t = n dt$, $n \in \{0, \dots, T_{\text{tot}}\}$, with T_{tot} the total number of simulated time steps. The discrete equation has the form

$$h(x, t + dt) - h(x, t) = -m_1 h(x, t) dt + \Delta_{x,t} (g_1 h + g_2 h^2 + g_3 h^3) dt + \xi(x, t) \quad (\text{S10})$$

where, at each time t and any point x , the noise $\xi(x, t)$ is independently drawn from a centered Gaussian distribution with variance dt . The operator $\Delta_{x,t}$ acting on a function f is defined by

$$\Delta_{x,t} f := \sum_{i=1,2} [2f(x, t) - f(x + \hat{e}_i, t) - f(x - \hat{e}_i, t)], \quad (\text{S11})$$

which is a common choice of discretization of the Laplace operator. Statistical averages $\langle \cdot \rangle$ are estimated by simulating the system R times with independent realizations of the noise and averaging over these repetitions. The value of the time increment dt must be chosen small enough to guarantee numerical stability of the integration algorithm. A value of $dt \leq 0.01$ is used in all simulations. The system is initialized at $h(x, t=0) = 0$ and is thermalized for a time $T_{\text{therm}} < T_{\text{tot}}$, after which measurements are made for a time $T := T_{\text{tot}} - T_{\text{therm}}$. The value of T_{therm} is established by measuring the variance $\frac{1}{N^2} \sum_x \langle h^2(x, t) \rangle$ at all times t . The latter grows over time, as noise adds more and more variability in the system, until it reaches a constant plateau value, becoming time-independent and thus signaling thermalization, see Fig. S1.

System size and correlation length Though the critical point is at $m_1 = 0$, in a realistic setting one must have a small, but finite mass m_1 . This for example prevents an unrealistic divergence of the variance of h and an infinite waiting time to reach thermalization. The mass implements a smooth lower momentum cut-off and thus defines a finite correlation length of $N_{\text{eff}} = \frac{2\pi}{m_1}$ lattice sites, which can be interpreted as the effective size of the system. Decreasing m_1 increases the effective system size N_{eff} . Alternatively, one can set $m_1 = 0$ and implement a hard momentum cut-off that only removes the $k = 0$ mode from the dynamics. Since the smallest available mode k_{min} then has $|k_{\text{min}}| = \frac{2\pi}{N}$, the correlation length is exactly $N_{\text{eff}} = \frac{2\pi}{k_{\text{min}}} = N$. Thus the extent of correlations is increased by increasing the size N of the system itself. Analytic predictions can be made in both cases and only differ by small minor corrections.

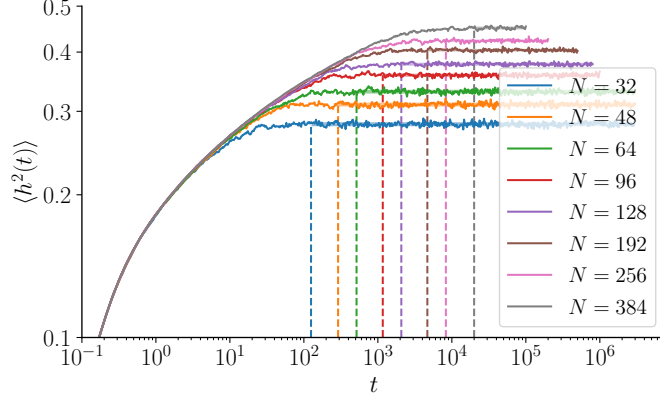


Figure S1. Measured space-averaged variance as a function of time for different system sizes. Dashed lines denote the thermalization time $T_{\text{therm}} dt$. Each curve represents an average over 256 trials.

We choose to present here the latter approach, as it makes for more elegant analytic expressions. The $k = 0$ cut-off is implemented at each time step t by subtracting from the noise its spatial mean $\xi(x, t) \rightarrow \xi(x, t) - N^{-2} \sum_x \xi(x, t)$, which in Fourier space corresponds to enforcing $\hat{\xi}(k = 0, t) = 0$. The noise term is indeed the only one contributing to the $k = 0$ mode in Eq. (S10): the two remaining terms are indeed one $\propto m_1 = 0$ and the other contains a Laplace operator, which in Fourier space is proportional to k^2 for $k \rightarrow 0$ and thus gives no contribution at $k = 0$.

Unphysical bi-stable regime Simulations are limited to the region $\bar{g}_2^2 < 3\bar{g}_3$, as an unphysical stationary state emerges for $\bar{g}_2^2 > 3\bar{g}_3$. This state has no physical interpretation, as it is just a consequence of the polynomial approximation of f , ceasing to be monotonically increasing for sufficiently large $|h|$, contrary to what is expected from a gain function in neural systems. This alternative stationary state has a checkerboard structure composed of two sublattices a and b , where the neural state variable assumes the values h_a and h_b , respectively. More precisely, a checkerboard structure means that if $h(x) = h_a$ then $h(x \pm \hat{e}_i) = h_b$, $\forall i = 1, 2$, and vice versa, exchanging $a \rightleftharpoons b$. The stationary state is defined in the absence of noise by the vanishing of the r.h.s. of Eq. (S10). With $m_1 = 0$, this gives the condition

$$g_1 h_a + g_2 h_a^2 + g_3 h_a^3 = g_1 h_b + g_2 h_b^2 + g_3 h_b^3. \quad (\text{S12})$$

The physical stationary state $h_a = h_b$ is always a solution of Eq. (S12). Additional solutions emerge if the third order polynomial in Eq. (S12) is not monotonically increasing. In this case $g_1 h + g_2 h^2 + g_3 h^3 = \text{const.}$ can have three different solutions, allowing for $h_a \neq h_b$. This occurs if

$$\frac{g_1 g_3}{g_2^2} < \frac{1}{3},$$

which translates to $\bar{g}_2^2 > 3\bar{g}_3$ for the dimensionless units. In simulations it turns out that the system is attracted to this unphysical state making simulations in this parameter regime meaningless.

A. Variance

From the simulated system, we measure the scaling of the variance of the field h with N . This is compared against our analytical prediction, in which the flow of the coupling g_1 introduces a logarithmic correction with respect to the linear case. Section IIA1 provides the details on how the variance was measured from simulations. Section IIA2 presents the derivation of the analytic prediction.

1. Measurement from simulation

From the simulated system, we measure the variance $\langle h^2(x, t) \rangle (N)$ for different lattice sizes N . This quantity is actually independent of both x and t , due to the spatio-temporal invariance of the system. Thus, we are able to

obtain a more refined measurement by additionally averaging over space

$$\langle h^2(t) \rangle := \frac{1}{N^2} \sum_x \langle h^2(x, t) \rangle,$$

and finally over time

$$\langle h^2 \rangle := \frac{1}{\bar{T}} \sum_t \langle h^2(t) \rangle. \quad (\text{S13})$$

To estimate the error $\sigma_{\langle h^2 \rangle}$ in measuring $\langle h^2 \rangle$, we use the variance of Eq. (S13) and divide by the number \bar{T} of statistically independent time samples:

$$\sigma_{\langle h^2 \rangle}^2 := \left[\frac{1}{\bar{T}} \sum_t (\langle h^2(t) \rangle - \langle h^2 \rangle)^2 \right] / \bar{T}. \quad (\text{S14})$$

The number \bar{T} is smaller than the total number T of time samples because two time samples can be considered statistically independent only when they are at a distance larger than the temporal correlation length. An estimate of this length is naturally given by the thermalization time $T_{\text{therm}} dt$, as this is the time after which the system completely forgets any initial condition. Using a conservative approach, we consider two time points to be independent when they are at a distance of $3T_{\text{therm}} dt$. Thus, the number of independent time samples we use is $\bar{T} := T / (3T_{\text{therm}})$. Fig. S1 illustrates the measured space-averaged variance $\langle h^2(t) \rangle$ and its thermalization over time t .

2. Prediction of variance by RG

The measured scaling of the variance with the system size N is compared against analytical predictions. The variance can be written as

$$\langle h^2 \rangle = \langle h^2(x=0, t) \rangle = \int \frac{d^2 k}{(2\pi)^2} \int \frac{d^2 k'}{(2\pi)^2} \langle \hat{h}(k, t) \hat{h}(k', t) \rangle. \quad (\text{S15})$$

We then use the scaling relation

$$\langle \hat{h}(k, t) \hat{h}(k', t) \rangle = \ell^{2\zeta} \langle \hat{h}_\ell(\ell k, \ell^{-2} t) \hat{h}_\ell(\ell k', \ell^{-2} t) \rangle_\ell, \quad (\text{S16})$$

where $\zeta = (d+2)/2 \stackrel{d=2}{=} 2$ is the scaling exponent of the field \hat{h} , as defined in the main text. The subscript ℓ in $\langle \rangle_\ell$ indicates that averaging must be performed according to the statistics defined by the effective theory at scale ℓ . We choose the highest possible value of the flow parameter $\ell = N/2$, so that all degrees of freedom have been marginalized in the effective theory, that is those with momenta $|k| \geq \frac{\Lambda}{\ell} = \frac{2\pi}{N} = |k_{\min}|$ (recall $k=0$ is removed from the dynamics). With this choice, no loop diagrams, which account for statistical fluctuations, contribute to the *r.h.s.* of Eq. (S16). This means only the tree level diagram of the form found in Eq. (S6) remains and thus

$$\ell^{2\zeta} \langle \hat{h}_\ell(\ell k, \ell t) \hat{h}_\ell(\ell k', \ell t) \rangle_\ell = \ell^2 \Delta_{\hat{h}_\ell \hat{h}_\ell}(\ell k, 0) \delta(k + k') = \frac{1}{2g_1(\ell) k^2} \delta(k + k').$$

The effect of fluctuations is hidden in the flown coupling $g_1(\ell = N/2)$. With this information, Eq. (S15) becomes

$$\langle h^2 \rangle = \int \frac{d^2 k}{(2\pi)^2} \ell^2 \Delta_{\hat{h}_\ell \hat{h}_\ell}(\ell k, 0) \Big|_{\ell=\frac{N}{2}} = \frac{1}{4\pi} \int_{\frac{2\pi}{N}}^{\pi} \frac{k dk}{g_1(N/2) k^2} = \frac{1}{4\pi} \frac{\ln(N/2)}{g_1(N/2)}. \quad (\text{S17})$$

In the second step, the angular part of the momentum integral is performed. Notice that the remaining radial integral starts from the lowest available mode $|k_{\min}| = \frac{2\pi}{N}$, thus giving the dependence of the variance on the correlation length (i.e. the system size N).

Eq. (S17) is strictly valid only in the limit of an infinite-size system, $N \rightarrow \infty$. Simulations are, however, restricted to finite values of N . To make a prediction that compares accurately with the simulated finite-sized systems, we need to apply some corrections to Eq. (S17). First, for finite N , the Fourier transformed fields \hat{h} are defined only on a

discrete, rather than continuous, set of momenta. These are $k = k_1 \hat{e}_1 + k_2 \hat{e}_2$, with $k_i = \frac{2\pi}{N} n_i$ and $n_i \in (\frac{N}{2} - 1, \frac{N}{2}) \cap \mathbb{Z}$. Thus the momentum integral in Eq. (S17) must be substituted with the sum

$$\frac{1}{N^2} \sum_k \xrightarrow{N \rightarrow \infty} \int \frac{d^2 k}{(2\pi)^2}. \quad (\text{S18})$$

Notice that the sum reduces to the integral when $N \rightarrow \infty$. Secondly, the propagator in Eq. (S17) must be substituted with its analogue for finite-size systems. This can be derived from the expression for the infinite-size system's propagator Eq. (S6). Notice that the k^2 appearing in the expression arises from the Fourier representation of the Laplace operator. Thus, one simply needs to substitute k^2 with the Fourier representation of the discrete Laplace operator Eq. (S11), which is $\sum_i (2 \cos(k_i) - 2)$. The finite-size propagator thus has the form

$$\Delta_{\hat{h}\hat{h}}(k, 0)^{-1} = 2g_1 \sum_i (2 \cos(k_i) - 2) \xrightarrow{k \rightarrow 0} 2g_1 k^2. \quad (\text{S19})$$

Notice that the finite-size propagator reduces to the infinite-size one in the limit of large wave-lengths $k \rightarrow 0$. In Eq. (S17), the propagator is that of the effective theory at scale $\ell = N/2$. This means the couplings appearing in the propagator must be evaluated at the point $\ell = N/2$ of their flow. In the infinite-size propagator, the only coupling appearing is g_1 ; but the finite-size propagator contains additional correction terms, each with its own coupling. We make these explicit by Taylor expanding the difference between the finite and infinite-size propagator

$$\Delta_{\hat{h}\hat{h}}(k, 0)^{-1} - 2g_1 k^2 := \sum_{n=4}^{\infty} c_n \sum_i k_i^n,$$

with the expansion coefficients c_n being the additional couplings. These are all of order $\mathcal{O}(k^4)$ and thus irrelevant: mean-field (i.e. dimensional) analysis predicts their flow to be $c_n(\ell) = \ell^{-(n-2)} c_n(0)$. We can assume this fast power-law decay to dominate their flow, and thus neglect higher order loop corrections. With this approximation, the flown propagator is given by

$$\begin{aligned} \ell^{-2} \Delta_{\hat{h}_\ell \hat{h}_\ell}(\ell k, 0)^{-1} &= 2g_1(\ell) k^2 + \sum_{n=4}^{\infty} c_n(\ell) \sum_i \ell^{n-2} k_i^n \\ &= 2g_1(\ell) k^2 + \sum_{n=4}^{\infty} c_n(0) \sum_i k_i^n \\ &= 2g_1(\ell) k^2 + 2g_1(0) \left[\sum_i (2 \cos(k_i) - 2) - k^2 \right]. \end{aligned} \quad (\text{S20})$$

We can finally plug the modifications Eqs. (S18) and (S20) into Eq. (S17) to obtain a finite-size system's prediction for the variance

$$\langle h^2 \rangle = \frac{1}{2N^2} \sum_{k \neq 0} \frac{1}{g_1(N/2) k^2 + g_1(0) [\sum_i (2 \cos(k_i) - 2) - k^2]}. \quad (\text{S21})$$

The sum over discrete momenta appearing in Eq. (S21) is carried out numerically.

B. Flow of the couplings

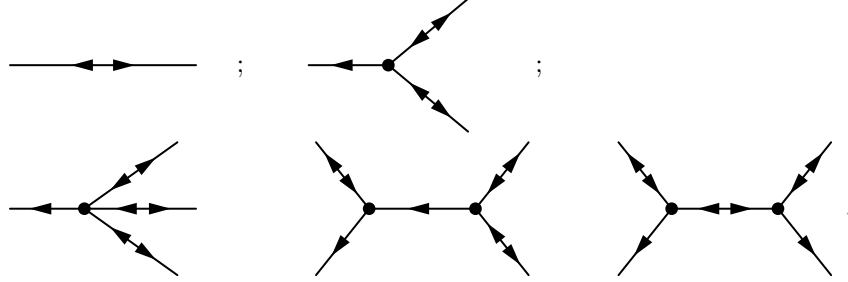
From the simulated system we also measure n -point correlations in momentum space up to $n = 4$, as a function of the correlation length (i.e. system size) N . These can be expressed in terms of the couplings $g_n(\ell)$ at $\ell = N/2$. This allows us, by varying the simulated system's size, to obtain a measured value of the couplings at different points of their flow. In Section II B 1 we derive the analytic expression relating correlations to the flown couplings. In Section II B 2 we detail how correlations are measured from simulations and the analytic expressions inverted to extract a measured value of the flown couplings.

1. Relationship between couplings and correlations

With the same reasoning as for the derivation of the variance Section II A 2, we make use of the scaling law

$$\langle\langle \hat{h}(k_1, t) \dots \hat{h}(k_n, t) \rangle\rangle = \ell^{n\zeta} \langle\langle \hat{h}_\ell(\ell k_1, \ell^{-2}t) \dots \hat{h}_\ell(\ell k_n, \ell^{-2}t) \rangle\rangle_\ell, \quad (\text{S22})$$

where $\zeta = (d+2)/2 \stackrel{d=2}{=} 2$ is the scaling exponent of the field \hat{h} , as defined in the main text, and $\langle\langle \rangle\rangle$ denotes cumulants, rather than moments. Evaluating at $\ell = N/2$, we only have to compute the r.h.s. of Eq. (S22) for a theory where all fluctuations have been integrated out. This means we get contributions from tree-level diagrams alone, and no loop diagrams, which would correspond to fluctuations. The diagrams contributing to the $n = 2, 3, 4$ -point correlation functions are respectively of the form


(S23)

Computed explicitly, these diagrams give the results

$$\langle\langle \hat{h}(k_1, t) \hat{h}(k_2, t) \rangle\rangle = \frac{D}{2g_1(N/2)k_1^2} \delta(k_1 + k_2), \quad (\text{S24})$$

$$\langle\langle \hat{h}(k_1, t) \hat{h}(k_2, t) \hat{h}(k_3, t) \rangle\rangle = -\frac{1}{2} \left(\frac{D}{g_1(N/2)} \right)^2 \frac{g_2(N/2)}{g_1(N/2)} \frac{\delta(k_1 + k_2 + k_3)}{k_1^2 + k_2^2 + k_3^2} \frac{k_1^2}{k_2^2 k_3^2} + perms, \quad (\text{S25})$$

$$\begin{aligned} \langle\langle \hat{h}(k_1, t) \dots \hat{h}(k_4, t) \rangle\rangle = & \left(\frac{D}{g_1(N/2)} \right)^3 \frac{\delta(k_1 + k_2 + k_3 + k_4)}{k_1^2 + k_2^2 + k_3^2 + k_4^2} \left(-\frac{1}{8} \frac{g_3(N/2)}{g_1(N/2)} \frac{k_1^2}{k_2^2 k_3^2 k_4^2} \right. \\ & + \frac{1}{4} \left(\frac{g_3(N/2)}{g_1(N/2)} \right)^2 \frac{(k_1 + k_2)^2 k_4^2}{k_1^2 k_2^2 k_3^2 \left((k_1 + k_2)^2 + k_4^2 + k_2^2 \right)} \\ & \left. + \frac{1}{4} \left(\frac{g_3(N/2)}{g_1(N/2)} \right)^2 \frac{k_2^2 k_4^2}{k_1^2 k_3^2 (k_1 + k_2)^2 \left((k_1 + k_2)^2 + k_1^2 + k_2^2 \right)} \right) + perms. \quad (\text{S26}) \end{aligned}$$

The notation $+perms$ means that the result is actually given by the sum of all permutations of momenta k_i in the expressions on the r.h.s of Eqs. (S25) and (S26). This corresponds to all possible ways of assigning momenta to the external legs of the diagrams in Eq. (S23).

2. Measurement of flown couplings from simulation

The measurement of the couplings $g_n(N/2)$ from the simulation follows the procedure described below. For each simulated time step t , the discrete Fourier transform $\hat{h}(t)$ of the measured state $h(t)$ is computed. Then, trial averaging is performed to estimate the cumulants on the l.h.s of Eqs. (S24) to (S26). These are only measured for momenta combinations satisfying the momentum conservation law $\sum_n k_n = 0$. For these combinations, the Dirac delta appearing on the r.h.s. of Eqs. (S24) to (S26) takes the value $\delta(0) = N^2$ (recall we consider a discrete system, so $\delta(0) \rightarrow \infty$ only for $N \rightarrow \infty$). Then, the values of $g_n(N/2)$ for $n = 1, 2, 3$ are extracted one after the other by inverting Eqs. (S24), (S25) and (S26). This gives a measured value of $g_n(N/2)$ for each momenta combination and time step. The flown couplings are, however, independent of these parameters so an additional averaging over momenta and time is performed. At the stage of time averaging, which is performed last, the statistical error is estimated, in the same way as is done for the variance measurement Section II A 1. Finally, we note that cumulants are only measured for small momenta $|k| < k_{max} = 0.44$. This is done because Eqs. (S24) to (S26) are only valid in the continuum limit $k \rightarrow 0$. In particular, the chosen value of k_{max} guarantees that the relative error between the discrete and continuous theory propagators, Eqs. (S19) and (S8), is at most 1.7% for the largest momenta.

C. Memory task

The simulated model is used as a reservoir computing system to perform a mnemonic task. The task is designed to measure the decay in the memory of a stimulus that is presented to the system.

The basic protocol comprises the following steps. First, the system evolves until time $t_{\text{in}} = T_{\text{therm}}$, reaching a thermalized state $h_0(x) := h(x, t_{\text{in}})$. Second, at time t_{in} a stimulus $s(x)$ consisting of a two-dimensional Gaussian shape is added on top of the thermalized state, $h(x, t_{\text{in}}) \rightarrow h(x, t_{\text{in}}) + s(x)$. The perturbed state $h(x, t)$ evolves further in time, still following Eq. (S10). Finally, at readout times $\{t_i | i = 1, \dots, n\}$ we take snapshots $h(x, t_i)$ and measure the accuracy $F(t_i)$ with which a trained linear readout can reconstruct the stimulus from $h(x, t_i)$. The reconstructed stimulus at time t_i is defined as

$$z(x, t_i) := \sum_{x'} W^{(i)}(x, x') h(x', t_i),$$

where $W^{(i)}$ is an $N^2 \times N^2$ readout weight matrix, whose entries $W^{(i)}(x, x')$ map a lattice point x' of the simulated system to a lattice point x of the reconstructed stimulus, cf. Fig. S2(a). We define the reconstruction error E , called *loss*, as the spatial mean over the squared difference between the stimulus and its reconstruction

$$E(t_i) := \frac{1}{N^2} \sum_x [z(x, t_i) - s(x)]^2,$$

which is equal to zero for perfect retrieval of the stimulus. Hence, $F(t_i) = 1 - E(t_i)/\mathcal{N}_i$, with \mathcal{N}_i some normalization factor, is a convenient measure for the reconstruction accuracy, as it has a maximum of 1 when the stimulus is perfectly reconstructed. The normalization factor is chosen such that the reconstruction accuracy is on average 0 when the stimulus has been completely forgotten by the system. This situation corresponds to the field $h(x, t_i)$ obeying the statistics of the thermalized, yet unperturbed state $h_0(x)$. In this case we have

$$\langle E(t_i) \rangle = \frac{1}{N^2} \sum_x [\langle z_0^2(x, t_i) \rangle + s^2(x)] =: \mathcal{N}_i \quad (\text{S27})$$

$$\text{with } z_0(x, t_i) := \sum_{x'} W^{(i)}(x, x') h_0(x', t_i),$$

where we used that $\langle z_0 \rangle = 0$. The statistical average appearing in Eq. (S27) is estimated within the training procedure outlined below. This indeed produces independent copies of the thermalized state h_0 which are used as trials to estimate $\langle z_0^2 \rangle$.

Training the readout We use gradient descent [10] to train the readout weight matrices W_i . To this end, we repeat the above protocol several times with different realizations of the noise I and in each iteration the weights are adjusted to minimize the loss. The gradient of the loss function with respect to the weights reads

$$\frac{\partial E(t_i)}{\partial W^{(i)}(x, x')} = \frac{2}{N^2} [z(x, t_i) - s(x)] h(x', t_i).$$

Therefore, the weight increment at each training step can be expressed as $\Delta W^{(i)}(x, x') = -\eta [z(x, t_i) - s(x)] h(x', t_i)$. All prefactors are absorbed into the adjustable learning rate η which has to be tuned such that the weights converge during the training. To achieve a faster and more robust convergence, we employ batch learning. One batch consists of multiple copies of the system and the readout weights. The copies are simulated in parallel with different noise realizations. After each training iteration, the gradient is computed for each copy and averaged over the batch. The averaged gradient is then used to update the weights. At the end of the training, the reconstruction accuracy of the last iteration, averaged over the batch, is stored. Batch averaging is also used to estimate $\langle z_0^2 \rangle$, which appears in the definition of the accuracy's normalization factor Eq. (S27). The whole training process is repeated several times with different noise realizations. The achieved accuracy's mean and standard deviation over these trials is computed.

D. Classification task

The simulated model is used as a reservoir computing system to perform a nonlinear classification task.

The task exploits the system's ability to perform nonlinear transformations to implement the parity function $p : \{-1, 1\}^\alpha \rightarrow \{0, 1\}$. It maps the binary representation $v \in \{-1, 1\}^\alpha$ of a given number to $p(v) = 1$ if and only

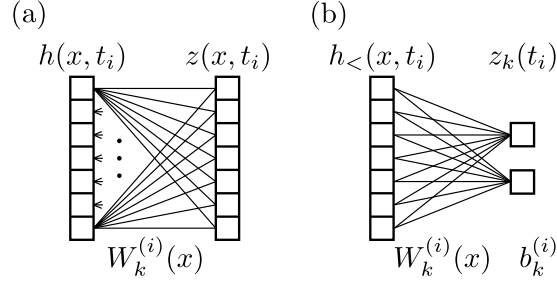


Figure S2. (a) Sketch of the readout at time t_i for the memory task. (b) Sketch of the readout at time t_i for the classification task.

if the number of ones in the input v is odd, and to $p(v) = 0$ otherwise. For the task presented in Fig. 2(b), we use $\alpha = 3$. The labeling according to the parity function is linearly non-separable, see main text Fig. 2(c).

The protocol of this task is similar to that of the memory task. The system evolves until a stationary state is reached, then a stimulus is added which encodes a binary representation v in a pattern consisting only of frequencies greater than a cutoff frequency k_{cut} . In our case we use $k_{\text{cut}} = \pi/2$. Details of the encoding are discussed below. Finally we use trained linear readouts at different times t_i to predict the parity of the stimulus. The readouts act on low-pass filtered snapshots $h_{<}(x, t_i)$. The snapshots $h_{<}(x, t_i)$ contain only frequencies smaller than k_{cut} so that the original stimulus is excluded and only the emerging lower modes are kept. This is done to further emphasize the role of nonlinearities in solving the task: not only are they needed to realize the mapping p , but also to transfer information from the higher modes where the input is fed to the lower modes from which the output is read out. The latter task is unsolvable for a linear system as modes are independent, which means that they cannot interact to transfer the information. For each t_i there are two readout units $z_k(t_i)$, $k = 1, 2$, defined by

$$z_k(t_i) = b_k^{(i)} + \sum_x W_k^{(i)}(x) h_{<}(x, t_i),$$

where the linear readout is performed by the weights $W_k^{(i)}(x)$, mapping a lattice point x to the readout unit k , and the biases $b_k^{(i)}$, causing an overall shift in the readout unit k , cf. Fig. S2(b). The two units represent the two classes of even ($k = 1$) and odd ($k = 2$) parity. Correspondingly, if $z_1(t_i) > z_2(t_i)$, the system's prediction is assumed to be "even", while it is "odd" in the opposite case. By repeating this procedure for all possible inputs several times with different noise realizations we compute the share of correctly classified inputs. As in the other task, we also perform the training several times and average over the results to get the mean and variance of the classification performance.

Representation of the input Each input ν is represented by a different stimulus $s_\nu(x)$. Each of its bit components $\nu_n \in \{-1, 1\}$, $n = 1, \dots, \alpha$, is represented by a spatial oscillation in the x_1 direction of frequency $\pi - n\delta k$ and amplitude ν_n , which are superimposed to give

$$s_\nu(x) = A \sum_{n=1}^{\alpha} \nu_n \cos((\pi - n\delta k) x_1),$$

with A some overall signal amplitude. The distance between the excited modes is given by $\delta k = 2\frac{2\pi}{N}$. Notice that, with $N = 128$ and $\alpha = 3$ as in Fig. 2(b), all stimuli contain only modes higher than the cutoff frequency $k_{\text{cut}} = \pi/2$.

Training the readout Again, we use gradient descent [10] to train the weights and biases. The loss function is the cross entropy error [11] defined by

$$E(t_i) = - \sum_k y_k^* \ln y_k(t_i),$$

where $y_k(t_i)$, $k = 1, 2$, is computed as the softmax of the bare output

$$y_k(t_i) = \frac{e^{z_k(t_i)}}{\sum_k e^{z_k(t_i)}}.$$

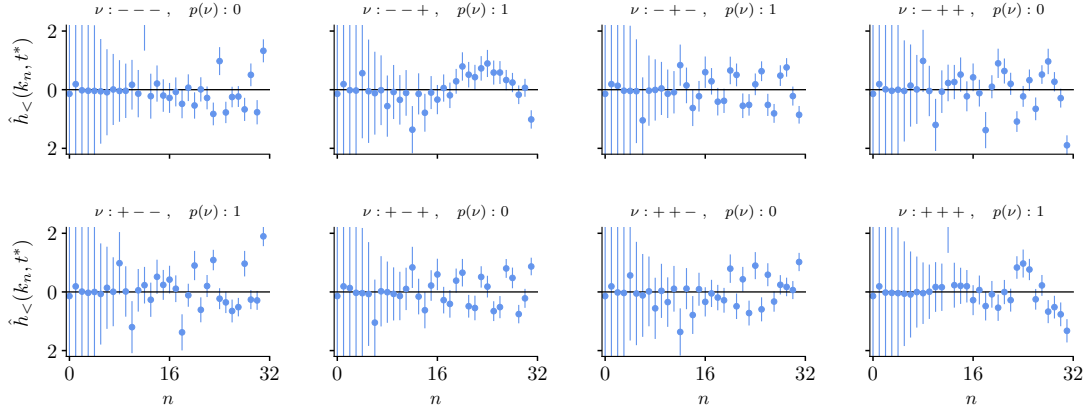


Figure S3. Diversity of patterns in the system's modes response to input stimuli. The Fourier transform $\hat{h}_<(k, t^*)$ of the low-pass filtered snapshots $h_<(x, t^*)$ used to train the readout in the classification task Fig. 2(b) is represented. The system size is $N = 128$ and $k_{\text{cut}} = \pi/2$; so only the modes $k_n = 2\pi n/128$, with $n = 0, \dots, 31$, pass the filter. Dots represent the real part of the Fourier transform along the x_1 direction averaged over 4096 trials (the stimulus is constant in x_2 direction so that this component does not carry any information). The vertical bars represent the standard deviation. The different panels show the emerging distribution of momentum modes in response to the eight different 3-bit strings. The readout time after input injection is $\Delta t = 0.5$.

The correct label is one-hot encoded in y^* , which means $y^* = (1, 0)^T$ if the input's parity is even and $y^* = (0, 1)^T$ otherwise. The gradients with respect to the biases and weights are given by

$$\begin{aligned} \frac{\partial E}{\partial W_{kl}^{(i)}}(t_i) &= (y_k(t_i) - y_k^*) h_<(t_i, x_l), \\ \frac{\partial E}{\partial b_k^{(i)}}(t_i) &= (y_k(t_i) - y_k^*). \end{aligned}$$

Also in this task we employ batch learning to make the training more robust.

Response of readout modes to stimuli In Fig. S3 we show the Fourier modes' response to the 8 different 3-bit strings. This shows the system's modes are interacting, with a degree of nonlinearity sufficient to perform the task. First, notice that all the lower modes that are used at readout respond to the input, which is originally fed to higher modes only. This requires interaction between modes to transfer information of the input, which is not possible in a linear system. Secondly, notice the diversity of patterns produced in response to the different 3-bit strings. This realizes the dimensionality expansion necessary to perform the task: from initially three dimensions, nonlinear interactions spread the inputs in the higher dimensional space of readout modes, such that a hyperplane in that space can be found that separates them correctly according to their parity.

E. Simulation parameters

Figure 1 The parameters of the simulations are the same for Fig. 1(b), (c), and (d) and depend only on the system size N . They are summarized in Table S1. The last row contains the order of magnitude of statistically independent measurements $R \cdot \bar{T}$ (recall \bar{T} is the number of statistically independent time steps; R is the number of repeated simulations of the system, with an independent realization of the noise). In all simulations $dt = 0.01$. The initial values in panel (b), denoted as tuples (\bar{g}_2^2, \bar{g}_3) , are given by (0.01, 0.1) (diamonds), (0.09, 0.1) (dots), (0.13, 0.066) (triangles), (0.109, 0.04) (squares). The data shown in panel (c) is obtained by multiplying the initial values of \bar{g}_2^2 and \bar{g}_3 by 15. In panels (b) and (c) the statistical error in the measurement of $\bar{g}_3(\ell)$ is represented by error bars. The same holds for $\bar{g}_2(\ell)$, but the error bars are too short to be resolved. The variance in panel (d) is computed for (0.01, 0.1), which is the same as the diamonds in (b). Again, the error bars are too short to be resolved.

Figure 2 The system size for the memory task in panel (a) is $N = 32$. Again, $dt = 0.01$ and $T_{\text{therm}} dt = 125$. Using a batch size of 48 and a learning rate $\eta = 0.01$, the training converged after 5000 iterations. The process is repeated five times to compute the average and standard deviation (error bars) of the reconstruction accuracy

N	32	48	64	96	128	192	256	384
$T_{\text{therm}}dt$	125	290	515	1165	2075	4665	8300	$2 \cdot 10^4$
$\# \text{samples}$	10^6	10^5	10^5	10^4	10^4	10^3	10^3	10^2

Table S1. Summary of the simulation parameters used to produce the results presented in Fig. 1 b, c, and d.

as described in Section II C. The stimulus $s(x)$ added on top of the thermalized system is a Gaussian $s(x) = A \exp\left(-(x_1 + x_2)^2 / (2\sigma^2)\right) / \sqrt{2\pi\sigma^2}$, where $A = 0.25$ and $\sigma = 0.2$.

For the parity task in panel (b), $T_{\text{therm}}dt = 2075$ is used, and a system of size $N = 128$, corresponding to 64 Fourier modes in each direction. We use $k_{\text{cut}} = \pi/2$, so that the lowest 32 modes are contained in the low-pass filtered snapshots. Equation Eq. (S7) shows that an excited mode decays $\propto \exp(-k^2t)$. The red, yellow, and green lines in Fig. 2 (b) show the decay of the modes $k = 2\pi n/128$, where $n \in \{1, 16, 32\}$, respectively. The stimuli, encoded in the high modes, introduce fluctuations on short spatial scales. For the algorithm to remain numerically stable, it is thus necessary to use a smaller simulation time step dt . Thus, we adapt the time step after the application of the stimulus from $dt = 0.01$ to $dt = 0.001$. The values of the interactions are given by $\bar{g}_2 = \bar{g}_3 = 0.3$. The signal amplitude is given by $A = 10.0$ and the learning rate $\eta = 0.025$. Using a batch size of 480, the training converged after 200 iterations. The mean and the variance of the share of correctly classified patterns is computed from eight trials.

III. COMPUTATION OF THE FLOW EQUATIONS

The flow equations (4)-(6) are computed to one-loop order within the framework of the infinitesimal momentum shell Wilsonian RG [12–14]. Once given the Feynman rules Eqs. (S5), (S6) and (S9), the procedure to derive the flow equations is well established. Still, identifying all the Feynman diagrams contributing to the equations and their combinatorial factor can be tedious and requires familiarity with the diagrams' properties that are specific to the model system. We thus list these diagrams here for completeness. We also calculate one of the diagrams in detail and use the example to point out properties of the diagrams that are specific to this field theory.

As an example, we consider the flow of g_1 . This is the coupling associated with a term $k^2\tilde{h}h$ in the action Eq. (S2). The one-loop contribution to the flow is thus given by all one-loop diagrams with exactly one \tilde{h} and one h -leg, that are amputated. These diagrams are

We are interested in the diagrams' contribution to the term $k^2\tilde{h}h$. This means we only want to compute them at 0-th order in ω . We therefore set $\omega = 0$. Also, we want to extract only the k^2 dependence of the diagrams, neglecting higher orders in k . To this end, we recall that at the critical point $m_n = 0$. From the vertices Eq. (S9) we then see that any diagram automatically carries a k^2 dependence for each of its external \tilde{h} -legs. As a result the k^2 dependence of the diagrams is simply given by the value of their internal loop at $k = 0$.

The diagrams' property above illustrated has two important consequences. The first is that it considerably simplifies the calculation of diagrams contributing to the flow of g_n , as we have seen for g_1 . The second is that no fluctuation correction contributes to the flow of couplings associated with terms of 0-th order in k . Indeed, any term in the action Eq. (S2) is at least proportional to one \tilde{h} and thus fluctuation corrections are at least of order k^2 . More specifically, the flow of D , τ and m_n is fully determined by mean-field analysis, as stated in the main text. Notice this is particularly important for the self-consistency of the whole argument, because we can say with certainty, already at mean-field level, that $m_n = 0$ at the critical point.

Coming back to the diagrams Eq. (S28), we compute explicitly the first one. We have to compute it for momenta

restricted to the thin momentum shell $\Lambda/\ell < |q| < \Lambda$. This gives

$$\begin{aligned}
 4 \cdot \text{diagram} &= 4g_2^2 \int \frac{d^2 q}{(2\pi)^2} \frac{d\nu}{2\pi} \Delta_{HH}(q, \nu) \Delta_{H\bar{H}}(q, \nu) q^2 \\
 &= 4g_2^2 \int \frac{d^2 q}{(2\pi)^2} \frac{d\nu}{2\pi} \frac{D}{\nu^2 + g_1^2 q^4} \frac{i}{\nu - ig_1 q^2} q^2 \\
 &= -\frac{D}{2\pi} \frac{g_2^2}{g_1} \int_{\Lambda/\ell}^{\Lambda} \frac{dq}{q} = -\frac{D}{2\pi} \frac{g_2^2}{g_1} \ln \ell.
 \end{aligned} \tag{S29}$$

The prefactor in front of the diagram is the combinatorial factor given by all possible ways of producing the diagram by contracting the vertices' legs. From the second to the last row, the ν -integral is computed using the residue theorem of complex analysis. Also the angular part of the momentum integral is computed, leaving only the radial part. Finally notice that we make a slight abuse of notation in Eq. (S29), as we compute only the internal loop of the diagram, that is excluding the k^2 dependence carried by the external \tilde{h} -leg.

Finally, we are interested in the diagram's contribution to the differential flow equation (4), that is to $\frac{1}{g_1} \frac{dg_1}{ds}$, with $s := (2\pi)^{-1} \ln(\ell)$. Thus we compute

$$\frac{2\pi}{g_1} \ell \frac{d}{d\ell} 4 \cdot \text{diagram} = -\frac{g_2^2}{g_1^2} \frac{D}{g_1} = -\bar{g}_2^2, \tag{S30}$$

which is indeed the second term on the r.h.s. of Eq. (4). We left implicit that the derivative by ℓ in Eq. (S30) must be computed at $\ell = 1$, which is the limit of an infinitesimal momentum shell.

In the following we give all the other diagrams contributing to the flow equations. There are two diagrams contributing to the flow of g_1 :

$$\ell \frac{d}{d\ell} \cdot 4 \cdot \text{diagram} = -\frac{D}{2\pi} \frac{g_2^2}{g_1^2} \quad \text{and} \quad \ell \frac{d}{d\ell} \cdot 3 \cdot \text{diagram} = \frac{3}{2} \frac{D}{2\pi} \frac{g_3}{g_1}.$$

The following four diagrams contribute to the flow of g_2 :

$$\begin{aligned}
 \ell \frac{d}{d\ell} \cdot 4 \cdot \text{diagram} &= -\frac{D}{2\pi} \frac{g_2^3}{g_1^3}, & \ell \frac{d}{d\ell} \cdot 8 \cdot \text{diagram} &= -\frac{D}{2\pi} \frac{g_2^3}{g_1^3}, \\
 \ell \frac{d}{d\ell} \cdot 8 \cdot \text{diagram} &= -\frac{D}{2\pi} \frac{g_2 g_3}{g_1^2}, & \ell \frac{d}{d\ell} \cdot 12 \cdot \text{diagram} &= -3 \frac{D}{2\pi} \frac{g_2 g_3}{g_1^2}.
 \end{aligned}$$

Finally, eight diagrams contribute to the flow of g_3 :

$$\begin{aligned}
 \ell \frac{d}{d\ell} \cdot 16 \cdot \text{Diagram 1} &= -\frac{D}{2\pi} \frac{g_2^4}{g_1^4}, & \ell \frac{d}{d\ell} \cdot 16 \cdot \text{Diagram 2} &= -3 \frac{D}{2\pi} \frac{g_2^4}{g_1^4}, \\
 \ell \frac{d}{d\ell} \cdot 12 \cdot \text{Diagram 3} &= 3 \frac{D}{2\pi} \frac{g_2^2 g_3}{g_1^3}, & \ell \frac{d}{d\ell} \cdot 24 \cdot \text{Diagram 4} &= 3 \frac{D}{2\pi} \frac{g_2^2 g_3}{g_1^3}, \\
 \ell \frac{d}{d\ell} \cdot 12 \cdot \text{Diagram 5} &= 3 \frac{D}{2\pi} \frac{g_2^2 g_3}{g_1^3}, & \ell \frac{d}{d\ell} \cdot 12 \cdot \text{Diagram 6} &= \frac{3}{2} \frac{D}{2\pi} \frac{g_2^2 g_3}{g_1^3}, \\
 \ell \frac{d}{d\ell} \cdot 12 \cdot \text{Diagram 7} &= \frac{3}{2} \frac{D}{2\pi} \frac{g_2^2 g_3}{g_1^3}, & \ell \frac{d}{d\ell} \cdot 12 \cdot \text{Diagram 8} &= -\frac{9}{2} \frac{D}{2\pi} \frac{g_2 g_3}{g_1^2}.
 \end{aligned}$$

and

-
- [1] P. Martin, E. Siggia, and H. Rose, Phys. Rev. A **8**, 423 (1973).
 - [2] C. De Dominicis, J. Phys. Colloques **37**, C1 (1976).
 - [3] J. A. Hertz, Y. Roudi, and P. Sollich, Journal of Physics A: Mathematical and Theoretical **50**, 033001 (2017).
 - [4] M. Helias and D. Dahmen, *Statistical Field Theory for Neural Networks*, vol. 970 (Springer International Publishing, 2020).
 - [5] J. Zinn-Justin, *Quantum field theory and critical phenomena* (Clarendon Press, Oxford, 1996).
 - [6] A. C. C. Coolen, arXiv:cond-mat/0006011 (2000).
 - [7] M. Gell-Mann and F. E. Low, Phys. Rev. **95**, 1300 (1954).
 - [8] K. G. Wilson, Rev. Mod. Phys. **47**, 773 (1975).
 - [9] P. E. Kloeden and E. Platen, *Numerical Solution of Stochastic Differential Equations* (Springer, Berlin, 1992).
 - [10] J. Kiefer and J. Wolfowitz, The Annals of Mathematical Statistics **23**, 462 (1952), ISSN 00034851.
 - [11] G. E. Hinton, Artificial Intelligence **40**, 185 (1989), ISSN 0004-3702.
 - [12] P. C. Hohenberg and B. I. Halperin, Rev. Mod. Phys. **49**, 435 (1977).
 - [13] E. Medina, T. Hwa, M. Kardar, and Y.-C. Zhang, Phys. Rev. A **39**, 3053 (1989).
 - [14] M. Helias, Journal of Physics A: Mathematical and Theoretical **53**, 445004 (2020).